Two-temperature treatments in magnetically arrested disk GRMHD simulations more accurately predict light curves of Sagittarius A*

L.D.S. Salas,[1]⋆ M.T.P. Liska,[2,3] S.B. Markoff,[1,4] K. Chatterjee,[5,6] G. Musoke,[7,1] O. Porth,[1] B. Ripperda,[7−10] D. Yoon,[11] W. Mulaudzi[1]

[1]*Anton Pannekoek Institute for Astronomy, University of Amsterdam, Science Park 904, 1098 XH Amsterdam, The Netherlands*
[2]*Center for Relativistic Astrophysics, Georgia Institute of Technology, Howey Physics Bldg, 837 State St NW, Atlanta, GA, 30332, USA*
[3]*Institute for Theory and Computation, Harvard University, 60 Garden Street, Cambridge, MA 02138, USA*
[4]*Gravitation and Astroparticle Physics Amsterdam Institute, University of Amsterdam, Science Park 904, 1098 XH 195 196 Amsterdam, The Netherlands*
[5]*Institute for Research in Electronics and Applied Physics, University of Maryland, 8279 Paint Branch Drive, College Park, MD 20742, USA*
[6]*Black Hole Initiative at Harvard University, 20 Garden Street, Cambridge, MA 02138, USA*
[7]*Canadian Institute for Theoretical Astrophysics, University of Toronto, 60 St. George Street, Toronto, ON M5S 3H8, Canada*
[8]*Dunlap Institute for Astronomy and Astrophysics, University of Toronto, 50 St. George Street, Toronto, ON M5S 3H4, Canada*
[9]*Department of Physics, University of Toronto, 60 St. George Street, Toronto, ON M5S 1A7, Canada*
[10]*Perimeter Institute for Theoretical Physics, 31 Caroline Street North, Waterloo, ON N2L 2Y5, Canada*
[11]*Information and Technology Services-Research Services, University of Iowa, Iowa 52242, Iowa City, IA 52242, USA*

ABSTRACT

The Event Horizon Telescope Collaboration (EHTC) observed the Galactic centre source Sagittarius A* (Sgr A*) and used emission models primarily based on single ion temperature (1T) general relativistic magnetohydrodynamic (GRMHD) simulations. This predicted emission is strongly dependent on a modelled prescription of the ion-to-electron temperature ratio. The most promising models are magnetically arrested disk (MAD) states. However, nearly all MAD models exhibit larger temporal fluctuations in radiative 230 GHz emission compared to observations. This limitation possibly stems from the fact that the actual temperature ratio depends on microphysical dissipation, radiative processes and other effects not captured in ideal fluid simulations. Therefore, we investigate the effects of two-temperature (2T) thermodynamics in MAD GRMHD simulations of Sgr A*, where the temperatures of both species are evolved. We find that the 230 GHz synchrotron flux variability more closely matches historical observations when we include the 2T treatment compared to 1T simulations. For the low accretion rates of Sgr A*, a common assumption is to neglect radiative cooling. However, we find that the radiative cooling of electrons—via synchrotron, inverse Compton, and bremsstrahlung processes—reduces the electron temperature in the inner disk, where the EHT observes, by about 10%, which, in turn, decreases both the (sub)millimetre synchrotron flux and its temporal fluctuations compared to uncooled simulations.

Key words: accretion, accretion discs – black hole physics — relativistic processes – MHD – methods: numerical – Galaxy: centre

1 INTRODUCTION

Sgr A* was discovered as a bright compact radio source in the centre of the Milky Way galaxy (Balick & Brown 1974; Ekers et al. 1975; Lo et al. 1975). Subsequent observations provided compelling evidence that this object is a supermassive black hole (SMBH) by analysing its proper motion and the dynamics of individual stars in orbit around it (Schödel et al. 2002; Ghez et al. 2003, 2008; Gillessen et al. 2009; GRAVITY Collaboration et al. 2018; Do et al. 2019; GRAVITY Collaboration et al. 2019). More recently, the Event Horizon Telescope Collaboration (EHTC) presented direct evidence for the presence of this SMBH via imaging of near-event horizon regions (EHTC Sgr A*2017 I; EHTC Sgr A*2017 VII). The accretion flow of Sgr A*

is collisionless based on the density inferred by, e.g., Yuan et al. 2003; Dexter et al. 2010; Bower et al. 2019; EHTC Sgr A*2017 V; EHTC Sgr A*2017 VIII. In collisionless plasmas, the electron-ion collision timescale is much longer than the accretion timescale, electrons and ions are decoupled and not in thermal equilibrium, such that they may have two different temperatures (2T) (Shapiro et al. 1976; Rees et al. 1982; Mahadevan & Quataert 1997; Quataert 1998). These accretion flows are typically modelled with ideal general relativistic magnetohydrodynamics (GRMHD), which does not capture its collisionless and 2T nature. The most common GRMHD models treat the fluid as composed of single temperature ions (1T), where the electron density and temperature are not considered in the evolution equations (e.g. Gammie et al. 2003; Tchekhovskoy et al. 2011; Narayan et al. 2012; McKinney et al. 2012). The (sub)millimetre emission is dominated by synchrotron radiation from relativistic electrons, making it

---

⋆ E-mail: l.d.sosapantasalas@uva.nl

crucial to accurately model electron thermodynamics. Ressler et al. (2015, 2017) introduced a method to evolve the GRMHD equations describing a gas consisting of ions and electrons that share the same dynamics but have independent thermodynamical evolution. In this so-called 2T treatment, there is only an additional electron entropy equation, while the particle number and energy-momentum equations continue to assume a single fluid (ions). Therefore, we investigate how incorporating this 2T treatment and the commonly ignored electron radiative cooling impacts the predicted (sub)millimetre variability from simulations of Sgr A*.

Decades of observations of Sgr A* give very strong constraints on the (sub)millimetre variability, which is usually quantified with the modulation index $M_3 \equiv \sigma_3/\mu_3$, where the standard deviation σ_3 and the mean μ_3 are measured over three hour time intervals of the light curve. Wielgus et al. (2022) used the Atacama Large Millimeter/submillimeter Array (ALMA) and the Submillimeter Array (SMA) as individual interferometers during the EHT observations on 2017 April 5–11. They studied the light curves of Sgr A* at four frequencies bands between 213 and 229 GHz, with a minimum cadence of approximately 10 s. They reported that Sgr A* exhibited a low flux density of 2.4 ± 0.2Jy and overall low variability, with non overlapping values $M_3 = [0.024 − 0.051]$ across April 5–10. On April 11, the ALMA observations immediately followed an X-ray flare, with a corresponding enhanced variability $M_3 = [0.084−0.117]$. The modulation index is consistent with other observations in 2005–2019 at frequencies around 230 GHz documented in various published works with longer cadence and lower number of collected data points (Marrone et al. 2006, 2008; Yusef-Zadeh et al. 2009; Dexter et al. 2014; Fazio et al. 2018; Bower et al. 2018; Witzel et al. 2021; Iwata et al. 2020; Murchikova & Witzel 2021).

1T GRMHD simulations include spherical accretion models (e.g. Ressler et al. 2021; Lalakos et al. 2024; Galishnikova et al. 2025), wid-fed models (Ressler et al. 2020, 2023), and torus-initialized models in the weakly magnetized (SANE) and magnetically arrested (MAD; Bisnovatyi-Kogan & Ruzmaikin 1974; Narayan et al. 2003) regimes. In the MAD regime the accretion is choked by the strong horizon penetrating magnetic field (e.g. Tchekhovskoy et al. 2011; Porth et al. 2021). In these 1T simulations the ion-to-electron temperature[1] ratio T_i/T_e is determined using the so-called $R(\beta)$ prescriptions (e.g. Mościbrodzka et al. 2016; Anantua et al. 2020), which is the main uncertainty in EHT modelling. None of the EHTC models of Sgr A* fully satisfy all the constraints drawn from multiwavelength observations at 86 GHz, 230 GHz, 2.2 μm, and in the X-ray (for a detailed explanation, see EHTC Sgr A*2017 II; EHTC Sgr A*2017 V). 230 GHz light curve variability at poses a particularly stringent challenge, as nearly all MAD models—and a significant portion of SANE models—exhibit greater variability ($M_3 \lesssim 0.5$) than seen in historical observations (Wielgus et al. 2022 and references therein). On the other hand, the more realistic stellar wind-fed accretion models better predict the submillimetre variability in Sgr A* due to the comparatively lower levels of small-scale turbulence compared to SANE and MAD models (Murchikova et al. 2022). This variability problem could potentially be attributed to not modelling the evolution of T_e when using the $R(\beta)$ prescriptions. In reality, T_e is fundamentally influenced by microphysical plasma and radiation interactions, and does not depend trivially on T_i. A first-principles kinetic approach is required to model these collisionless effects (Parfrey et al. 2019; Crinquand et al. 2022; Galishnikova et al. 2023a). Nonetheless, it is possible to effectively model the electron thermodynamics of thermal

electrons with 2T treatments in extended GRMHD simulations (e.g. Ressler et al. 2015) and by including radiative effects (e.g. Sądowski et al. 2017; Chael et al. 2018).

The mechanisms of heating in collisionless plasma remain largely unconstrained. Typically used heating models include prescriptions for weakly collisional turbulent cascades (Howes 2010, H10; Kawazura et al. 2019, K19) and magnetic reconnection mechanisms (Rowan et al. 2017, R17; Rowan et al. 2019, R19). These heating models have limited applicability, as reconnection and turbulence likely occur in diverse conditions across the disk and jet, making it improbable for a single, universally applied model to capture their complexity. Sądowski et al. (2017); Ryan et al. (2015, 2017); Chael et al. (2018, 2019); Liska et al. (2024) implemented the 2T treatment in a GR radiation MHD (GRRMHD) scheme with coupling between gas, radiation, magnetic fields and gravity. This 2T treatment does not capture realistic dissipative heating (see section 2.1). When assuming that ions and electrons are heated through magnetic reconnection (R17 model), it was demonstrated that electrons are always cooler than ions and that electron heating is more uniform (Chael et al. 2018). Additionally, the R17 model was favoured in a polarimetric parameter survey of Sgr A*, comparing H10, K19 and R17 (Dexter et al. 2020). Because of the 2T nature of the accretion flow, a gas mixture consisting of relativistic electrons with an adiabatic index $\gamma_e = 4/3$ and non-relativistic ions with $\gamma_i = 5/3$ was found for the mass accretion rate of Sgr A* and R17 model (Chael et al. 2018; Liska et al. 2024). As a result, assuming a single fixed value for the gas adiabatic index could lead to inconsistencies between the total and individual temperatures and pressures. The adiabatic index characterizes the fluid response to compression, relating gas pressure p_g and density ρ via $p_g \propto \rho^\gamma$. Distinct adiabatic indices are important because electron thermodynamics govern observable emissions, while ion dynamics influence the bulk flow. Therefore, it is crucial to conduct a detailed comparison between the evolved T_e from 2T GRMHD simulations with variable adiabatic indices and the T_e calculated using the $R(\beta)$ prescription.

The estimated Eddington ratio[2] of Sgr A* is $f_{edd} \equiv \dot{M}/\dot{M}_{edd} \sim [1 − 100] \times 10^{-8}$ (e.g. Agol 2000; Bower et al. 2003; Marrone et al. 2007). A common assumption for Sgr A* is that radiative cooling and transport do not have a significant impact on the accretion dynamics and (sub)millimetre emission. In the advection-dominated accretion flow (ADAF) model, the radiative efficiency η_{rad} is less than 0.001 at all radii, meaning that less than 0.1% of the available accretion energy is radiated (Narayan & Yi 1994; Narayan et al. 1995). Fragile & Meier (2009); Dibi et al. (2012) were pioneers in incorporating electron radiative cooling processes (Esin et al. 1996), including bremsstrahlung, synchrotron, and inverse Compton, into simulations. When $f_{edd} > 10^{-7}$ for a 1T GRMHD SANE state, electron cooling lowers the scale-height of the accretion disk and the overall flux of the spectra from the submillimetre to the far-UV (Drappeau et al. 2013; Yoon et al. 2020). Similarly, variations in T_i/T_e were identified when $f_{edd} \gtrsim 10^{-7}$ in a 2T treatment (Dihingia et al. 2023). For a SANE state, radiation has a negligible effect on either the dynamics or the thermodynamics of the accreting gas when $f_{edd} \sim 2 \times 10^{-8}$ (Sądowski et al. 2017). Radiative cooling was found to lower T_e in the inner regions of the accretion flow for $f_{edd} > 10^{-6}$ in SANE

---

[1] T_i is the ion temperature and T_e is the electron temperature.

[2] $\dot{M}$ is the mass accretion rate, $\dot{M}_{edd} = 4\pi GM/(c\kappa_{es}\eta_{NT})$ is the Eddington accretion rate, M is the mass of the black hole, κ_{es} is the opacity due to electron scattering, and $\eta_{NT} = 0.178$ is the radiative efficiency of a thin accretion disk with black hole spin $a = 0.9375$ (Novikov & Thorne 1973). For Sgr A*, $\dot{M}_{edd} \approx 0.05 M_\odot/\text{yr}$.

states (Ryan et al. 2015, 2017). On the other hand, a MAD state has significantly higher level of magnetic flux and therefore higher η_{rad} due to more efficient synchrotron emission. When $f_{edd} \approx 10^{-7}$, $\eta_{rad} \approx 0.03$ for a MAD state and $\eta_{rad} \approx 0.002$ for a SANE state (Liska et al. 2024). Therefore, radiative cooling may be important for simulating Sgr A* if the accretion flow is in a MAD state.

In this paper, we study the variability of synchrotron radiative emission at [43-1360] GHz predicted from 2T GRRMHD simulations in a MAD state. We include variable adiabatic index (Sądowski et al. 2017), and radiative cooling of electrons (synchrotron, inverse Compton, and bremsstrahlung; Esin et al. 1997) appropriate for Sgr A*. In our implementation, the cooling source terms subtract energy and momentum (see section 2.1; Fragile & Meier 2009; Dibi et al. 2012). Synchrotron emission dominates the radiative cooling rates and flux at [43-1360] GHz (Yoon et al. 2020). We also include Coulomb coupling that characterizes the transfer of energy between ions and electrons that occurs through collisions in a kinetic manner (see appendix A; Stepney & Guilbert 1983). Additionally, we assume that electron/ion heating occurs via magnetic reconnection (R17 model), and we do not account for anisotropic thermal conduction along magnetic field lines, as considered in Ressler et al. (2015). Recent studies have incorporated similar or more advanced physics at lower grid resolutions (Chael et al. 2018; Dexter et al. 2020; Ressler et al. 2023). However, an analysis of variability that systematically adds one layer of physics at a time has been lacking. We quantify the variability of the total synchrotron flux density using the three-hour modulation index M_3. Our results show that the inclusion of 2T treatment, variable adiabatic index, and cooling systematically shifts the M_3 distribution towards lower variability values at 86, 228, 345, and 1360 GHz.

The structure of this paper is as follows: Section 2 provides the 2T GRMHD equations and numerical setup for our simulations. The results of electron radiative cooling, heating, variable adiabatic index, and ray tracing are discussed in Section 3. The conclusions of the study are presented in Section 4.

2 SIMULATIONS

2.1 2T GRMHD equations

We use geometrized units with gravitational constant, black hole mass, and speed of light $G = M = c = 1$, and a factor of $1/\sqrt{4\pi}$ is absorbed in the definition of the magnetic field. The gravitational radius is $r_g \equiv GM/c^2$. Greek indices run through $[0, 1, 2, 3]$ and Roman indices through $[1, 2, 3]$. The metric determinant is g. A semicolon ; is used to represent a covariant derivative. In the M1 closure scheme implemented in Sądowski et al. (2017); Chael et al. (2018); Liska et al. (2024), radiation (approximated as a fluid) and gas are coupled through the exchange of four-momentum, a process known as radiative transport. We do not include the radiation energy-momentum equation, i.e., we neglect radiative transport. Instead, we solve the equations of GRMHD that comprise the particle number conservation equation:

$$\left(nu^\mu\right)_{;\mu} = 0 \, , \tag{1}$$

the energy-momentum conservation equations:

$$T^\mu{}_{\nu;\mu} = u_\nu q^- \, , \tag{2}$$

and the Maxwell's equations:

$$F^{*\mu\nu}{}_{;\nu} = 0 \, . \tag{3}$$

In ideal MHD, the dual of the electromagnetic field tensor is $F^{*\mu\nu} = b^\mu u^\nu - b^\nu u^\mu$ and the stress-energy tensor is:

$$T^\mu{}_\nu \equiv \left(\rho + u_g + p_g + b^2\right) u^\mu u_\nu - b^\mu b_\nu + \left(\frac{1}{2}b^2 + p_g\right)\delta^\mu{}_\nu \, , \tag{4}$$

here n is the particle number density, $\rho = nm_p$ is the rest mass density[3], m_p is the proton mass, u_g is the gas energy density, p_g is the gas pressure, and $b^2/2$ is the magnetic energy density. The 4-velocity and the magnetic field 4-vector are u^μ and b^μ respectively. $\delta^\mu{}_\nu$ is the Kronecker delta. The gas pressure is proportional to the gas temperature ($p_g \propto T_g$). The magnetic pressure is $p_b = b^2/2$, where b is the magnetic field strength in the frame co-moving with the fluid. q^- is the radiative cooling rate of electrons (see section 3.1). We assume that proton cooling is insignificant, as proton synchrotron emission is negligible in the (sub)millimetre regime (e.g. Event Horizon Telescope Collaboration et al. 2022c). We consider a purely hydrogen fluid, so the relative mass abundances of hydrogen and helium are $X = 1$ and $Y = 0$. Therefore, the number densities are $n_e = n_i = n$.

Single fluid GRMHD assumes that both electrons and ions move at the same bulk velocity $u_e^\mu = u_i^\mu = u^\mu$, so their momenta are considered separately. The first law of thermodynamics determines the evolution of the species entropies,

$$T_e \left(n_e s_e u^\mu\right)_{;\mu} = \delta_e q^v + q^C + q^- \, , \tag{5}$$

$$T_i \left(n_i s_i u^\mu\right)_{;\mu} = \delta_i q^v - q^C \, , \tag{6}$$

where $s_{e,i}$ and $T_{e,i}$ are the entropy per particle and temperature of electrons and ions, respectively. $q^v = q_e^v + q_i^v$ is total dissipative heating rate (or "viscous" heating rate), $\delta_e = q_e^v/q^v$ and $\delta_i = 1 - \delta_e$ the electron- and ion-to-overall heating ratio, and q^C is the Coulomb coupling rate (energy exchange between electrons and ions).

The entropy per particle of an ideal gas with fixed adiabatic index γ is $s \propto \ln(p/\rho^\gamma)$. We follow the approach in Sądowski et al. (2017), and use an approximate relativistic entropy formula,

$$s_{e,i} = k_B \ln \left[\frac{\Theta_{e,i}^{3/2} \left(\Theta_{e,i} + 2/5\right)^{3/2}}{\rho_{e,i}} \right] \, , \tag{7}$$

which is analytically invertible for the dimensionless temperature $\Theta_{e,i} = k_B T_{e,i}/m_{e,i}c^2$, where k_B is the Boltzmann constant. The ideal gas equation of state provides the means to determine the effective temperature of the gas T_g, which is a mix of electrons and ions,

$$p_g = \left(\gamma_g - 1\right) u_g = \frac{k_B \rho}{m_p} T_g \, . \tag{8}$$

The electron temperature T_e is obtained from the entropy density equation 5. Both species satisfy the equation of state,

$$p_{e,i} = \left(\gamma_{e,i} - 1\right) u_{e,i} = \frac{k_B \rho}{m_p} T_{e,i} \, , \tag{9}$$

The gas pressure/energy is the sum of the electron and ion pressures/energies, $p_g = p_e + p_i$ and $u_g = u_e + u_i$. Therefore, the temperatures must satisfy, $T_g = (T_e + T_i)/2$, and the effective adiabatic index of the mixture is,

$$\gamma_g = 1 + \frac{(\gamma_e - 1)(\gamma_i - 1)(T_i/T_e + 1)}{(T_i/T_e)(\gamma_e - 1) + (\gamma_i - 1)} \, , \tag{10}$$

---

[3] Normalised to a maximum density $\rho_{max} = 1$ for the 1T simulation.

Table 1. Setup parameters and simulation outcomes at quasi-steady state.

Name	Cooling	Adiabatic index[a]	$\rho_s(\text{cgs})/10^{-19}$	$F(\nu)$[b]/Jy	$f_{\text{edd}}^{\text{c}}/10^{-7}$	$t_{\text{f}}(10^3 r_g/c)$
1T	off	$\gamma_i = 5/3$	-	-	-	29.1
2T	off	$\text{var}(\gamma)$	2.7	3.2	1.0	32.7
2TC	on	$\text{var}(\gamma)$	2.7	2.7	1.0	29.1
2TC-8.3Jy	on	$\text{var}(\gamma)$	4	8.3	2.2	15.4
2TC-17.9Jy	on	$\text{var}(\gamma)$	10	17.9	4.2	21.2
2TC-93.8Jy	on	$\text{var}(\gamma)$	10^2	93.8	38.6	21.5
2TC-62.0Jy	on	$\text{var}(\gamma)$	10^3	62.0	365.1	21.1

[a] $\text{var}(\gamma)$ represents variable adiabatic index (Sądowski et al. 2017). [b] Time-averaged synchrotron flux density at 228 GHz. [c] Time-averaged Eddington ratio measured at the event horizon.

where $\gamma_{e,i}$ are the electron and ion adiabatic indices (Narayan et al. 2011; Sądowski et al. 2017),

$$\gamma_{e,i} \approx \frac{10 + 20\Theta_{e,i}}{6 + 15\Theta_{e,i}} . \tag{11}$$

We follow the method of Ressler et al. (2015) to numerically identify the total dissipative heating q^{v} by evolving the thermal entropies adiabatically over a time step $\Delta\tau$. By comparing the sum of the adiabatically evolved energy densities, $u_{i,\text{ad}}$ and $u_{e,\text{ad}}$, to the separately evolved total gas energy u_g, we estimate the dissipative heating in the total fluid as $q^{\text{v}} = (u_g - u_{i,\text{ad}} - u_{e,\text{ad}})/\Delta\tau$. The numerical implementation of mixing finite-sized fluid parcels into a single homogenised fluid within a cell artificially increases the entropy of the gas, which should not be treated as dissipation. As a result, this method loses accuracy in regions of the accretion flows with large discontinuities, such as those found in MAD states (for more details, see Sądowski et al. 2017; Chael 2025). This method does not capture real dissipation. In reality, the physical processes that produce dissipation occur at scales much smaller than the simulation grid. We do not explicitly model the heating mechanisms via effective resistivity or viscosity. Instead, we assume that heating at the grid scale occurs through sub-grid magnetic reconnection (Rowan et al. 2017).

2.1.1 Heating

Previous studies on grid-scale dissipation have considered mainly two heating prescriptions: turbulent heating and magnetic reconnection. The non-relativistic turbulent heating model H10 was originally developed for solar wind observations and is based on calculations of a turbulent cascade in a weakly collisional plasma with $\sigma_i \ll 1$ (Howes 2010). The relativistic turbulent heating model K19 exhibits quantitatively similar behaviour to the H10 model (Kawazura et al. 2019). For Sgr A*, assuming H10 results in a negligible difference in electron temperatures in MAD models compared to K19 (Dexter et al. 2020).

We adopt the heating of electrons and ions resulting from magnetic reconnection with zero guide field (Rowan et al. 2017; Chael et al. 2018). This model is based on particle-in-cell simulations with physical mass ratio $m_i/m_e = 1836$ and total magnetisation for relativistic particles, that properly accounts for relativistic inertia $\sigma_{\text{w}} = b^2/\text{w} \geqslant 0.03$. The electron-to-overall heating ratio δ_e is

$$\delta_e = 0.5 \exp\left[\frac{\beta_i/\beta_{i,\text{max}} - 1}{0.8 + \sigma_{\text{w}}^{0.5}}\right], \tag{12}$$

where the enthalpy density per unit volume is $\text{w} = \rho_i c^2 + \gamma_e u_e + \gamma_i u_i$. The ratio of ion thermal pressure to magnetic pressure is $\beta_i =$

$2k\rho_i T_i/\left(m_i b^2\right)$, where $\beta_i \leqslant \beta_{i,\text{max}} = 1/(4\sigma_{\text{w}})$. The heating prescription including the effect of guide fields by Rowan et al. (2019) is quantitatively similar to zero guide field case Eq. 12. Unlike H10, Eq. 12 varies less rapidly with β_i, is always non-zero and never allocates more than half of the heat to electrons.

2.2 Numerical setup

We perform the GRMHD simulations using the H-AMR code (Liska et al. 2022), which builds on the HARM2D code (Gammie et al. 2003; Noble et al. 2006). H-AMR employs GPU acceleration within a hybrid CUDA-OpenMP-MPI framework, integrating adaptive mesh refinement (AMR) and local adaptive time-stepping (LAT) to facilitate efficient and scalable simulations. We use spherical Kerr–Schild coordinates, where t, r, θ and ϕ are the temporal, radial, polar and azimuthal coordinates, respectively. The number of cells in the radial, polar and azimuthal directions are $N_r \times N_\theta \times N_\phi = 520 \times 224 \times 224$. The radial domain is $r = [1.2 - 2000] \, r_g$. We use outflow boundary conditions in r, transmissive boundary conditions in θ, and periodic boundary conditions in ϕ, as described in Liska et al. (2022). In all runs the disk is initialised using a torus in hydrostatic equilibrium (Fishbone & Moncrief 1976) around a Kerr black hole with dimensionless spin $a = 0.9375$. The initial inner edge of the torus is located at $r = 20r_g$ and the pressure maximum at $r = 41r_g$. The torus is threaded with a single poloidal magnetic field loop, defined by the ϕ-component of the vector potential $A_\phi \propto \max\left[\rho/\rho_{\text{max}} (r/r_{\text{in}})^3 \sin^3\theta \exp(-r/400) - 0.2, 0\right]$, and normalised to obtain $\beta = p_g/p_b = 100$ at pressure maxima, specifically to reach a MAD state. The following floor and ceiling values are employed; the rest-mass density floor is $\rho_{\text{fl}} = \max[b^2/25, 10^{-7}r^{-2}, 10^{-20}]$, the gas energy density floor is $u_{g,\text{fl}} = \max[b^2/750, 10^{-9}r^{-26/9}, 10^{-20}]$ and the magnetisation ceiling is $\sigma_{\text{max}} = 25$ where $\sigma = b^2/\rho$. The disk is initialised with the same energy density perturbation $u_g(1 + 0.04(\text{rand}([0,1]) - 0.5))$, where $\text{rand}([0,1])$ is a random deviate between 0 and 1.

For the 1T simulation, we assume a non-relativistic gas with a constant adiabatic index of 5/3. Table 1 summarises the main simulation setup parameters, and results of 228 GHz flux density and Eddington ratio. The 1T simulation is scale-free, whereas the 2TC simulations require a density scale ρ_s to compute the physical radiative cooling rates. To obtain the appropriate density scale, we performed an iterative process: running multiple 2TC simulations, performing raytracing, and verifying the time-averaged flux density at 228 GHz. The 2TC simulation (without extra labels) matches the 228 GHz flux density 2.7 Jy (EHTC Sgr A*2017 II). The 2TC-x.xJy simulations were initialized with higher density scales, resulting in higher accretion

rates and increased 228 GHz synchrotron flux densities, $F(\nu) > 8$Jy. A higher plasma density increases opacity, thereby reducing synchrotron flux variability. Therefore, we compare the variability of synchrotron radiative emission only between simulations 1T, 2T and 2TC with 2.7Jy. 2TC follows the same initial setup as 2T but with cooling enabled. The values reported in Table 1 and Section 3 for simulation 2T are obtained using the same density scale as in simulation 2TC. The primary simulations (1T, 2T, 2TC) are evolved for a time of approximately $3 \times 10^4 r_g/c$, with a cadence of $10 r_g/c$, equivalent to 3.5 minutes for Sgr A*.

3 RESULTS

In order to determine quantitative differences between the simulations we compare various fluid parameters. The averaged profile of a variable X is calculated by integrating over θ and ϕ. The accretion flow is taken to be the region that satisfies magnetisation $\sigma = b^2/\rho < 1$. Additionally, we include a density weight to give more relevance to regions of the disk with higher density and therefore higher thermal synchrotron emissivity $j_\nu = j_\nu(\rho, B, T_e)$, [4]

$$\langle X \rangle_{\rho[\theta,\phi]}^{\text{disk}} = \frac{\iint X \rho \, (\sigma < 1) \, \sqrt{-g} d\theta d\phi}{\iint \rho \, (\sigma < 1) \, \sqrt{-g} d\theta d\phi} \, . \tag{13}$$

The fluxes are defined as follows. The mass accretion rate $\dot{M}$ is given by:

$$\dot{M} \equiv - \iint \rho u^r \sqrt{-g} d\theta d\phi \, , \tag{14}$$

the energy flux $\dot{E}$ is given by:

$$\dot{E} \equiv - \iint T^r{}_t \sqrt{-g} d\theta d\phi \, , \tag{15}$$

the magnetic flux is defined as:

$$\Phi \equiv \frac{\sqrt{4\pi}}{2} \iint |B^r| \sqrt{-g} d\theta d\phi \, . \tag{16}$$

For $r \lesssim 100 r_g$, there is an inflow equilibrium in the disk so $\dot{M}_{\text{disk}}$ is approximately constant. The disk properties still depend on the initial conditions of the Fishbone-Moncrief torus for radii larger than $100 r_g$. To study MAD simulations it is convenient to use the normalised magnetic flux, $\varphi \equiv \Phi / \sqrt{\langle \dot{M} \rangle}$, known as the "MAD parameter" which, for spin $a = 0.9375$ and torus scale height $H/R \approx 0.3$, has the critical value $\varphi_{max} \approx 40 - 50$ (when using cgs units in the ratio; Tchekhovskoy et al. 2012). For SANE models, $\varphi_{max} \approx 7$ (Chatterjee & Narayan 2022). H and R are the full height and cylindrical radius of the disk, respectively. The scale height is defined geometrically as $H/R \equiv \langle |\theta - \pi/2| \rangle_{\rho[\theta,\phi]}^{\text{disk}}$. In general, subscripts indicate where in the radial domain the variables are analysed, e.g. X_{BH} at the event horizon and X_{10r_g} at $10 r_g$.

3.1 Radiative cooling

The total cooling rate for an optically thin gas is computed from the cooling function,

$$q^- = \eta_{\text{br,C}} \, q_{\text{br}}^- + \eta_{\text{Sync,C}} \, q_{\text{Sync}}^- \, , \tag{17}$$

---

[4] Note the difference in notation, $\langle \rangle$ without any sub/super script is time average.
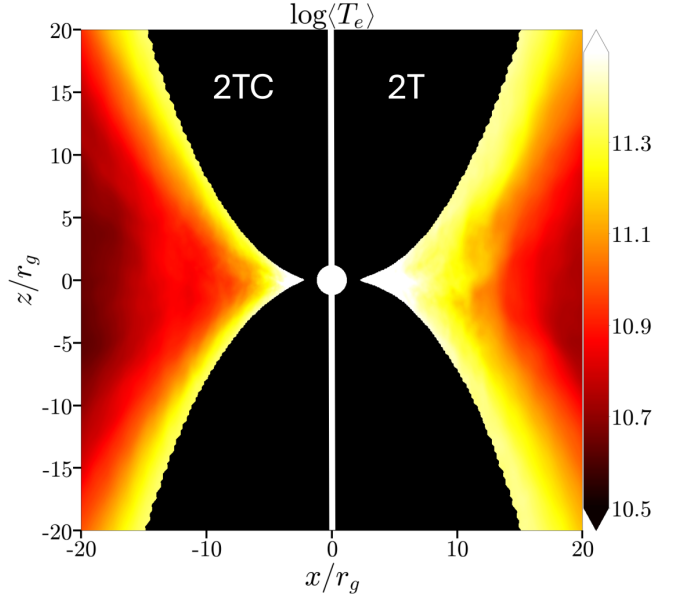

Figure 1. Cross sections in the xz-plane at $y = 0$ showing (log) electron temperature in Kelvin, averaged between $[16 - 29] \times 10^3 r_g/c$. 2T with cooling (left) and without cooling (right). Radiative cooling lowers the electron temperature in the inner accretion disk. We cover the jet spine region ($\sigma > 1$) with a black screen.
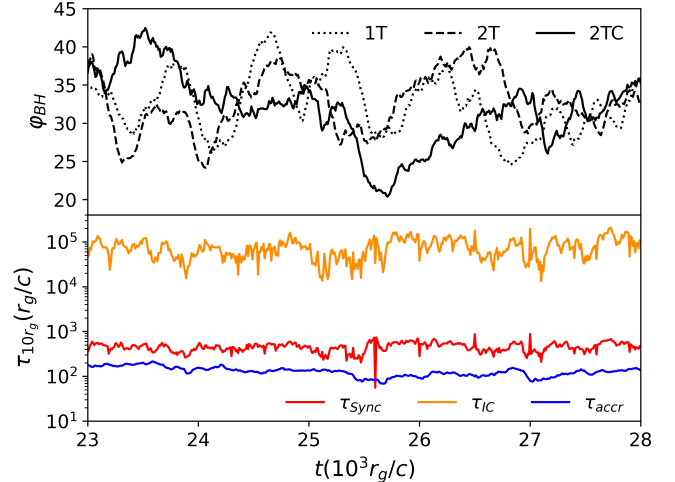

Figure 2. Normalised magnetic flux (top panel) and various timescales (bottom panel) as functions of time. The magnetic flux saturates after $t = 5 \times 10^3 r_g/c$. Line conventions are as follows: 1T—dotted, 2T—dashed, 2TC—solid. Timescales for synchrotron emission (τ_{Sync}), Comptonization (τ_{IC}), and accretion (τ_{accr}) at $10 r_g$ highlight the relative significance of these processes.

where q_{br}^- and q_{Sync}^- are the bremsstrahlung and synchrotron cooling rates, respectively. We find that Bremsstrahlung cooling is negligible, consistent with Yoon et al. (2020). $\eta_{\text{br,C}}$ and $\eta_{\text{Sync,C}}$ are the Compton enhancement factors for bremsstrahlung and synchrotron, respectively. These factors are the average energy gain of the photon in an assumption of single scattering (Esin et al. 1996). A detailed description of the cooling rates is available in Yoon et al. (2020).

Fig. 1 shows a comparison of T_e for simulations 2T and 2TC. Even for the very low accretion rate relevant for Sgr A*, $f_{\text{edd}} \approx 10^{-7}$, we find that radiative cooling still lowers T_e in the inner disk and the
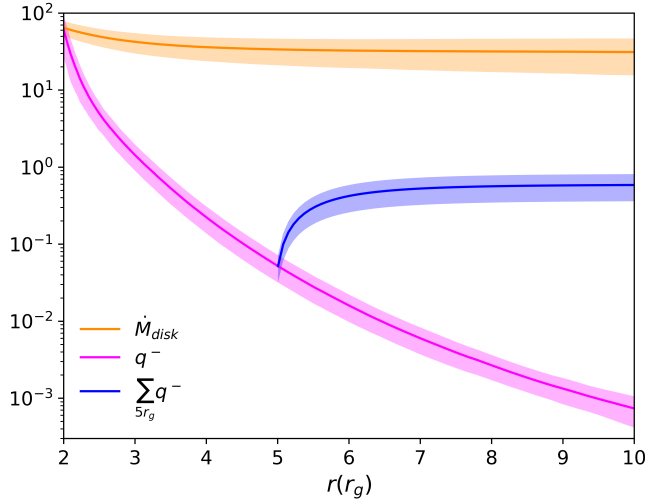
Figure 3. Disc averaged profiles of the total cooling rate q^-, and mass accretion rate $\dot{M}_{disk}$, averaged between $[23-28]\times10^3 r_g/c$. Shaded regions depict the range of variation within one standard deviation. The estimated radiative efficiency is $\eta_{rad} \approx 0.02 \pm 0.1$.

average synchrotron flux by 10% (see Table 1). The importance of the radiative losses is tested by computing the radiative cooling timescale $\tau = u_e/q^-$ and compare it to the dynamical accretion timescale. We calculate the synchrotron timescale as:

$$\tau_{\text{Sync}} \equiv \frac{\langle u_e \rangle^{\text{disk}}_{\rho[\theta,\phi]}}{\left\langle q^-_{\text{Sync}} \right\rangle^{\text{disk}}_{\rho[\theta,\phi]}} , \tag{18}$$

the Comptonization timescale as:

$$\tau_{\text{IC}} \equiv \frac{\langle u_e \rangle^{\text{disk}}_{\rho[\theta,\phi]}}{\left\langle (\eta_{\text{Sync,C}} - 1) q^-_{\text{Sync}} \right\rangle^{\text{disk}}_{\rho[\theta,\phi]}} , \tag{19}$$

and the accretion timescale as:

$$\tau_{\text{accr}} \equiv \frac{\iint \rho r \sqrt{-g}\, d\theta d\phi}{\left\langle \dot{M}_{10r_g} \right\rangle} . \tag{20}$$

MAD states are characterised by large fluctuations caused by episodic magnetic flux eruptions. Once magnetic flux becomes over-saturated, magnetic reconnection occurs near the black hole, ejecting low-density, highly magnetised flux tubes into the disk (e.g. Porth et al. 2021; Chatterjee et al. 2021; Ripperda et al. 2022). Fig. 2 presents time series between $[23 - 28] \times 10^3 r_g/c$ of the normalised magnetic flux and the previously defined timescales. Across all simulations, the average flux $\langle \varphi \rangle \approx 35$ reveals distinct signatures of several magnetic flux eruption events. Our analysis indicates that the timescales, ranked by relevance, are as follows: synchrotron $\langle \tau_{\text{Sync}} \rangle / \langle \tau_{\text{accr}} \rangle \sim 3$, and Comptonization $\langle \tau_{\text{IC}} \rangle / \langle \tau_{\text{accr}} \rangle \sim 500$. Therefore, we find that synchrotron emission dominates over inverse Compton, consistent with Yoon et al. (2020); Liska et al. (2024).

In 2T GRRMHD simulations, Liska et al. (2024) demonstrated that magnetic flux significantly influences radiative efficiency, primarily attributed to more efficient synchrotron emission in MAD models at low accretion rates (see also Ryan et al. 2017; Dexter et al. 2021). At $f_{\text{edd}} \approx 10^{-7}$, $\eta_{\text{rad}} \approx 0.002$ and $T_i/T_e \approx 10$ at $10r_g$ in the disk for SANE models, while for MAD models, $\eta_{\text{rad}} \approx 0.03$ and $T_i/T_e \approx 3$ at $10r_g$ in the disk (Liska et al. 2024). Their more

self-consistent calculation of radiative efficiency incorporates the radiation stress-energy tensor in the M1 scheme. In our simulations, which include only radiative cooling, we estimate the radiative efficiency $\eta_{\text{rad}} \approx \eta_{\text{NT}} (\tau_{\text{accr}}/\tau_{\text{cool}})_{10r_g} \approx 0.05 \pm 0.1$, where $\tau_{\text{cool}} = (1/\tau_{\text{Sync}} + 1/\tau_{\text{IC}})^{-1}$. Alternatively, using the cooling rate $\eta_{\text{rad}} \approx \sum_{5r_g}^{200r_g} q^- / \left\langle \dot{M}_{5r_g} \right\rangle \approx 0.02 \pm 0.01$ (see Fig. 3).

3.2 Heating and variable adiabatic index

Fig. 4 shows the correlation between the magnetisation (σ_w), ion plasma beta (β_i), and the electron-to-overall heating ratio δ_e determined by Eq. 12. In general, δ_e determines the temperature and adiabatic index of both species and the gas mixture (see Eq. 5, 6, 10, and 11). By assuming heating through magnetic reconnection, we observe the increase of T_e more prominently in regions with high σ_w and low β_i. In those regions, the adiabatic index of the electron/ion mixture, determined by T_e and T_i, approaches 4/3, consistent with the plasma becoming relativistic as a result of heating. The 1T simulation employs a fixed value of 5/3. During an eruption in MAD states, the expulsion of magnetic flux goes through the magnetic reconnection of field lines in a current sheet in the equatorial plane. Highly magnetised plasma from the jet spine region ($\sigma = b^2/\rho > 1$) supplies matter to the current sheet, with $T \propto \sigma_{\text{max}}$, and the reconnection exhaust deposits this hot plasma in the jet-disk interface (Ripperda et al. 2022).

In the first-principles kinetic simulations of (Rowan et al. 2017), magnetic energy is transformed into heat or kinetic energy when magnetic fields reconnect. This process accelerates and heats particles, with electron heating being particularly prominent in regions where magnetic pressure is high, like in the disk-jet boundary and flux tubes during episodes of magnetic flux eruption events. In GRRMHD SANE simulations of Sgr A*, Chael et al. (2018) demonstrated that electrons are preferentially heated in the polar outflows with the H10 prescription (see also e.g. Sądowski et al. 2017; Ressler et al. 2017), whereas electrons are heated by nearly the same fraction everywhere in the accretion flow with the R17 prescription. Additionally, the models assuming the R17 heating model show variability in the 230 GHz light-curve more consistent with the level observed from Sgr A* (Wielgus et al. 2022 and references therein).

Fig. 5 shows radial profiles of the scale-height, adiabatic indices, electron and ion temperatures, and the synchrotron, Comptonization, and accretion timescales (see section 3.1). Our findings reveal that the scale-height in 1T simulations is larger compared to the 2T and 2TC simulations, but within the one standard deviation range. The higher adiabatic index in the 1T simulation results in a higher T_i and a larger scale-height. Comparing the 2T and 2TC simulations, we find that radiative cooling reduces T_e by approximately 15% within $50r_g$, with the most significant drop occurring between $[30 - 50]r_g$. This cooling effect also lowers the values of γ_e and γ_g. We find that while the radial profile of the timescale ratio $\tau_{\text{Sync}}/\tau_{\text{accr}}$ remains relatively constant, $\tau_{\text{IC}}/\tau_{\text{accr}}$ increases significantly with increasing radius.

We observe a temperature ratio of $\langle T_i/T_e \rangle \approx 3$ and $\langle T_e \rangle \sim 10^{11}$ K, both time averaged between $[16 - 29] \times 10^3 r_g/c$ and measured at $10r_g$, consistent with those reported in 2T simulations (e.g. Liska et al. 2024), and in spectral fitting modelling of 1T simulations where the ion-to-electron temperature ratio is a model parameter (e.g. Mościbrodzka et al. 2009; Drappeau et al. 2013). Mościbrodzka et al. (2009) found that models with $T_i/T_e = 1$ were inconsistent with the submillimeter spectral slope, while those with $T_i/T_e = 3$ and 10 provided a better match to spectral and VLBI observations. Furthermore, with the inclusion of radiative cooling (Dibi et al. 2012),
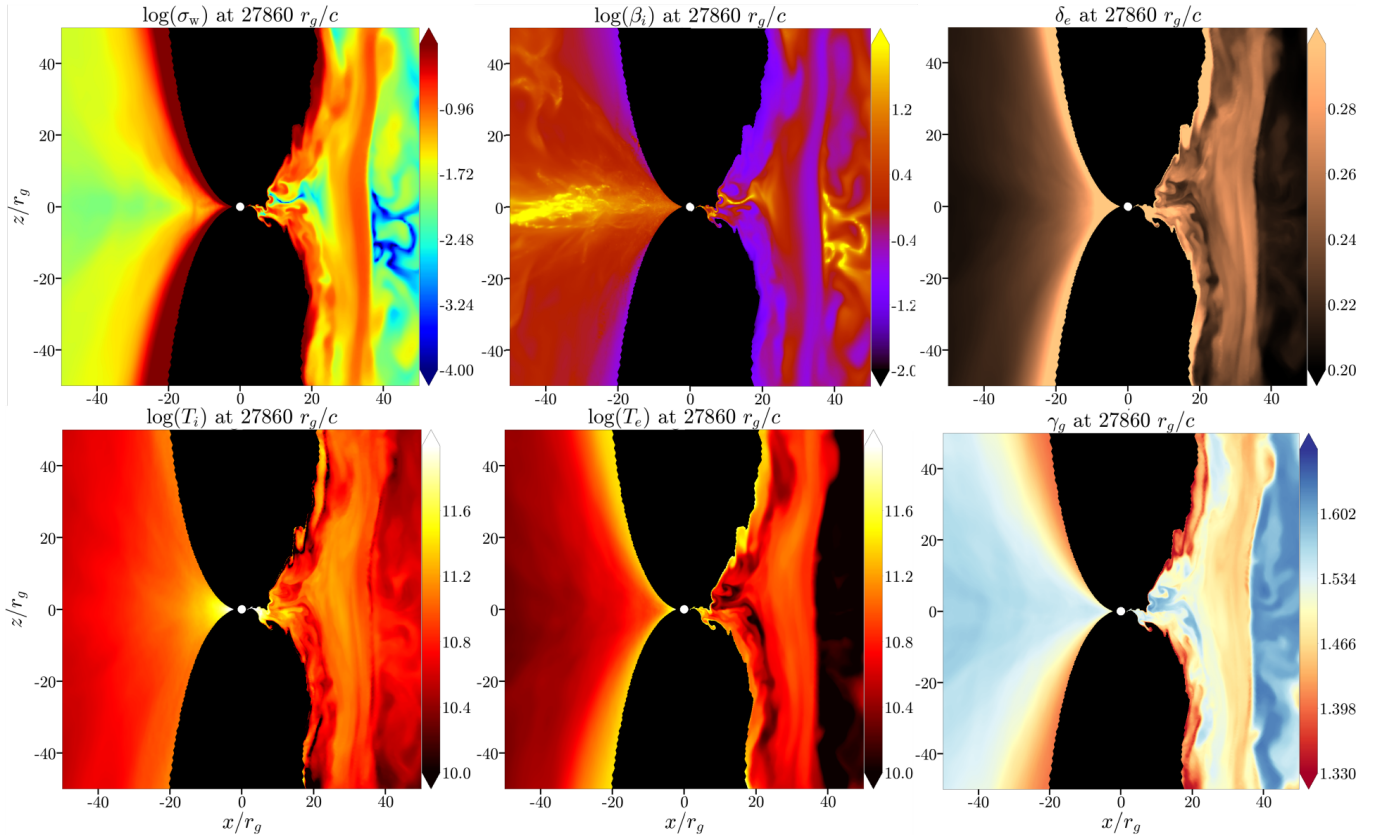
Figure 4. Cross sections in the xz-plane at $y = 0$ during a episode of magnetic flux eruption in simulation 2TC. First row: (log) total magnetisation σ_w (left panel), (log) ion plasma beta β_i (middle panel) and electron-to-overall heating ratio δ_e (right panel). Second row: (log) ion temperature in Kelvin T_i (left), (log) electron temperature T_e in Kelvin (middle) and adiabatic index of gas mixture (right). The left hemispheres show the time-averaged values between $[16 - 29] \times 10^3 r_g/c$ including flux eruptions, while the right hemispheres present a snapshot at $27860 r_g/c$. We cover the jet spine region ($\sigma > 1$) with a black screen. Electron heating is particularly prominent in the jet-disk interface and flux tubes, where magnetic pressure is high (high σ_w and low β_i). The evolved T_e surpasses T_i in the jet-disk interface. The time-averaged $\gamma_g \approx 1.55$ at $20 r_g$. During a flux eruption, the temperatures in the jet-disk interface depend on the magnetisation ceiling as $T \propto \sigma_{\max}$ (Ripperda et al. 2022).

Drappeau et al. (2013) identified an optimal spectral fit for models with $T_i/T_e = 3$.

3.3 Ray Tracing

The ray-tracing of the GRMHD simulations is performed by solving the general-relativistic radiative transfer (GRRT) equations using the BHOSS code (Younsi et al. 2012, 2016). Radiative processes are calculated using synchrotron emission and absorption, which are sufficient for imaging and light curve analysis across radio and sub-millimetre frequencies. In the submillimetre regime, synchrotron emission dominates the spectrum (Yoon et al. (2020); EHTC Sgr A*2017 V). The 2.2 μm emission is usually dominated by synchrotron, and the X-ray can be dominated by either Compton scattering or bremsstrahlung (EHTC Sgr A*2017 V). To match the average synchrotron flux density of Sgr A* at 2.7 Jy at 228 GHz (EHTC Sgr A*2017 II), the density scale is adjusted in the GRRT post-processing of the 1T simulation. For the 2T models, the density scale is directly obtained from the GRMHD simulations (see Table 1).

Based on the mean values of Sgr A* reported by Do et al. (2019) and GRAVITY Collaboration et al. (2019), we assume the mass $M = 4.14 \times 10^6 M_\odot$ (same as in the 2T simulations) and distance $D = 8.127$kpc, where $M_\odot$ is the solar mass (EHTC Sgr A*2017 V). Since there is no definitive evidence of a jet in Sgr A*, determining

the exact orientation of the source relative to our line of sight remains challenging. Nevertheless, the model comparison of the EHTC suggests that high inclination angles ($i > 50°$) are unlikely (EHTC Sgr A*2017 V). We analyse the 1T simulation considering six inclination angles, $i = [10, 30, 50, 130, 150, 170]°$, and the 2T simulations with the preferred value $i = 30°$ that passes most total intensity and polarimetric constraints (EHTC Sgr A*2017 V; EHTC Sgr A*2017 VIII). We find that M_3 distributions do not significantly depend on the inclination angle.

In the 1T simulation, the strength of electron–proton coupling is unknown, yet T_e is crucial to calculate the radio synchrotron spectra assuming a thermal electron distribution function. Similarly as in Mościbrodzka et al. (2016, 2017), we calculate T_e using the parametrization with respect to the plasma beta ($\beta \equiv p_g/p_b$),

$$\frac{T_i}{T_e} \equiv R_{\text{high}} \frac{\beta^2}{\beta^2 + 1} + R_{\text{low}} \frac{1}{\beta^2 + 1} . \tag{21}$$

This $R(\beta)$ model was initially developed phenomenologically for SANE simulations and may not be suitable for MAD states, particularly in predicting submillimetre light curves. In regions of the accretion flow where $\beta \gtrsim 1$ or $\lesssim 10^{-2}$, the electron temperature is approximately independent of β. Consequently, T_e fluctuates approximately as much as T_i (see section 3.4).

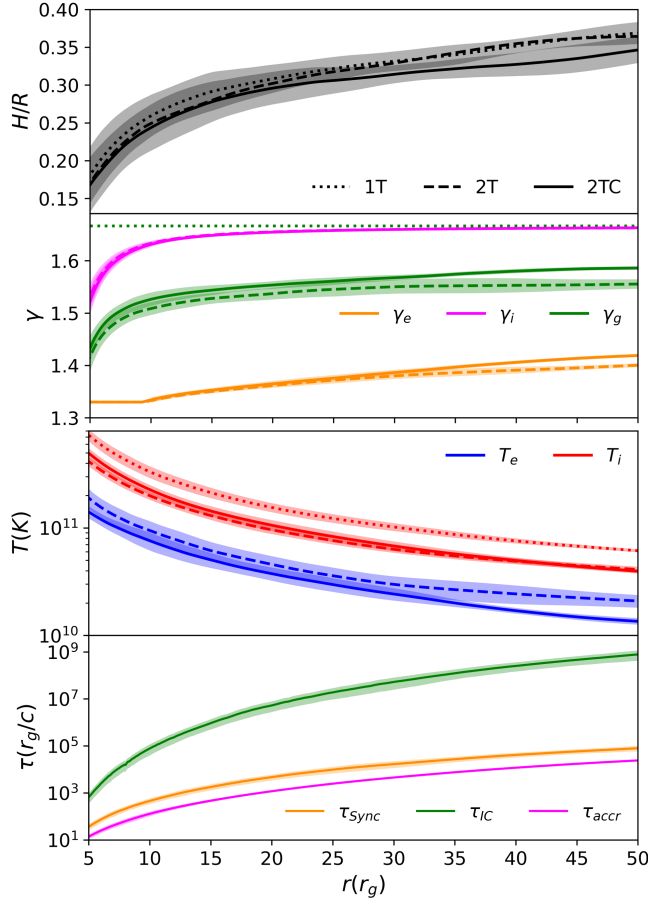For Sgr A*, electron distribution functions with approximately

Figure 5. Disc averaged profiles of variables as a function of radius, averaged between $[22 - 29] \times 10^3 r_g/c$. First panel: density scale-height. Second panel: adiabatic indices. Third panel: electron and ion temperatures. Fourth panel: timescales at $27860 r_g/c$. Line conventions are as follows: 1T—dotted, 2T—dashed, 2TC—solid. Shaded regions depict the range of variation within one standard deviation. Inflow equilibrium is better converged in the final part of the simulation. Despite cooling lowers T_e, the thickness of the disk at $< 15 r_g$ remains unchanged because ion and magnetic pressures dominate over electron pressure. Lower adiabatic index values correspond to reduced pressure and temperature.

equal proton and electron temperatures ($R_{high} = 1$) are unlikely based on the 2017 data observed by the EHT, and the two most promising models have $R_{high} = 160$ (EHTC Sgr A*2017 V; EHTC Sgr A*2017 VIII), so that the electrons are much colder in the disk and hotter in the jet. However, 2T GRMHD simulations with H10, K19 and R17 heating prescriptions have consistently shown that time averaged $T_i/T_e \approx [3 - 10]$ in the accretion disk (e.g. Chael et al. 2018; Mizuno et al. 2021; Dihingia et al. 2023; Liska et al. 2024). The sole value of $R_{low} = 1$ explored by the EHTC could potentially skew the high values of R_{high}. When $f_{edd} \approx 10^{-6}$ and $a = 0.94$, Mizuno et al. (2021) found that MAD models using the R17 heating prescription show only a slight reduction in 230 GHz light-curve variability compared to predictions from 1T simulations using the $R(\beta)$ prescription. Moscibrodzka (2024) demonstrated that 2T MAD models with K19 heating exhibit less variability at 228 GHz compared to $R(\beta)$ models, even when using a constant gas adiabatic index of $\gamma = 13/9$. Additionally, M_3 increases with black hole spin and slightly decreases when physics of non-thermal electrons are included. Moreover, their

Table 2. Mean and standard deviation values of M_3 for the 1T simulation. M_3 increases with R_{high} but does not significantly depend on the inclination angle.

R_{high}	i	M_3	$\langle f_{edd} \rangle /10^{-8}$	$\langle P_{jet} \rangle /10^{38} \mathrm{erg/s}$
160	10	0.26 ± 0.09	39.2	5.9 ± 1.5
160	30	0.26 ± 0.08	39.9	6.6 ± 1.7
160	50	0.27 ± 0.07	40.4	6.2 ± 1.6
160	130	0.27 ± 0.07	40.8	6.2 ± 1.6
160	150	0.27 ± 0.08	40.2	6.1 ± 1.6
160	170	0.26 ± 0.09	39.3	6.0 ± 1.0
40	30	0.24 ± 0.08	19.8	3.0 ± 0.8
20	30	0.23 ± 0.09	15.7	2.3 ± 0.6
10	30	0.21 ± 0.09	11.2	1.7 ± 0.4
1	10	0.18 ± 0.08	6.9	1.1 ± 0.3
1	30	0.17 ± 0.08	6.8	1.1 ± 0.3
1	50	0.17 ± 0.08	6.4	1.1 ± 0.3
1	130	0.18 ± 0.08	6.8	1.1 ± 0.3
1	150	0.18 ± 0.08	6.9	1.1 ± 0.3
1	170	0.18 ± 0.08	6.9	1.1 ± 0.3

resolved images most closely resemble 1T models with $T_i/T_e = 10$ in both linear and circular polarisation.

We explore five values $R_{high} = [1, 10, 20, 40, 160]$. We find that the evolved T_e surpasses T_i in the jet-disk interface (see Fig. 4), whereas the T_e calculated using the $R(\beta)$ prescription invariably remains lower than T_i. Fig. 6 shows a visual comparison of the ray-traced images at inclination $i = 30°$ for simulations 2TC and 1T at different frequencies. Images from the 2T simulation are not included in Fig. 6, as they are nearly identical to those from the 2TC simulation. The density scales to match the time-averaged flux density of 2.7 Jy are $\rho_{scale} = 2.6$ and $15.4\,(\mathrm{g\,cm}^{-3})$ for $R_{high} = 1$ and 160, respectively. As R_{high} increases, emission from the disk ($\beta > 1$) diminishes while emission from the rapidly moving outflows ($\beta < 1$) intensifies. This effect results in increased synchrotron flux variability, as shown in Table 2.

Table 2 also presents the jet power $P_{jet} = \dot{M}_{jet} - \dot{E}_{jet}$, averaged over the region between 50 and $500 r_g$, where the jet is identified based on the Bernoulli parameter $Be = -\bar{h}u_t > 1.02$ where $\bar{h} = (\rho + u_g + p_g)/\rho$ is the specific gas enthalpy and u_t is the time component of the inverse four-velocity (Davelaar et al. 2018). The density scale derived from ray-tracing the 1T simulations is used to calculate the jet power in cgs units. For comparison, the jet power in the 2TC and 2T simulations is $(1.4 \pm 0.4) \times 10^{38} \mathrm{erg/s}$ and $(1.3 \pm 0.3) \times 10^{38} \mathrm{erg/s}$, respectively, which matches with the jet power in the 1T simulation for R_{high} between 1 and 10.

We obtain distributions of the modulation index M_3 measured over three-hour intervals. Fig. 7 shows the 228 GHz light curves and M_3 distributions[5] for $i = 30°$. Values of M_3 for the 1T simulation with different inclination angles and R_{high} are presented in Table 2. A comparison of M_3 at different frequencies for 1T, 2T and 2TC simulations is presented in Table 3. We find that the 2T treatment, variable adiabatic index and radiative cooling shifts the M_3 distribution towards lower variability values. However, historical observations of Sgr A* (Wielgus et al. 2022 and references therein) still show lower M_3 values than 2T simulations.

From the 2T and 2TC simulations, we extract two light curve

---

[5] The EHT observes in four frequency bands centred at 213.1 GHz (band 1), 215.1 GHz (band 2), 227.1 GHz (band 3), and 229.1 GHz (band 4). The M_3 values at 228 GHz and 230 GHz are indistinguishable in our simulations.
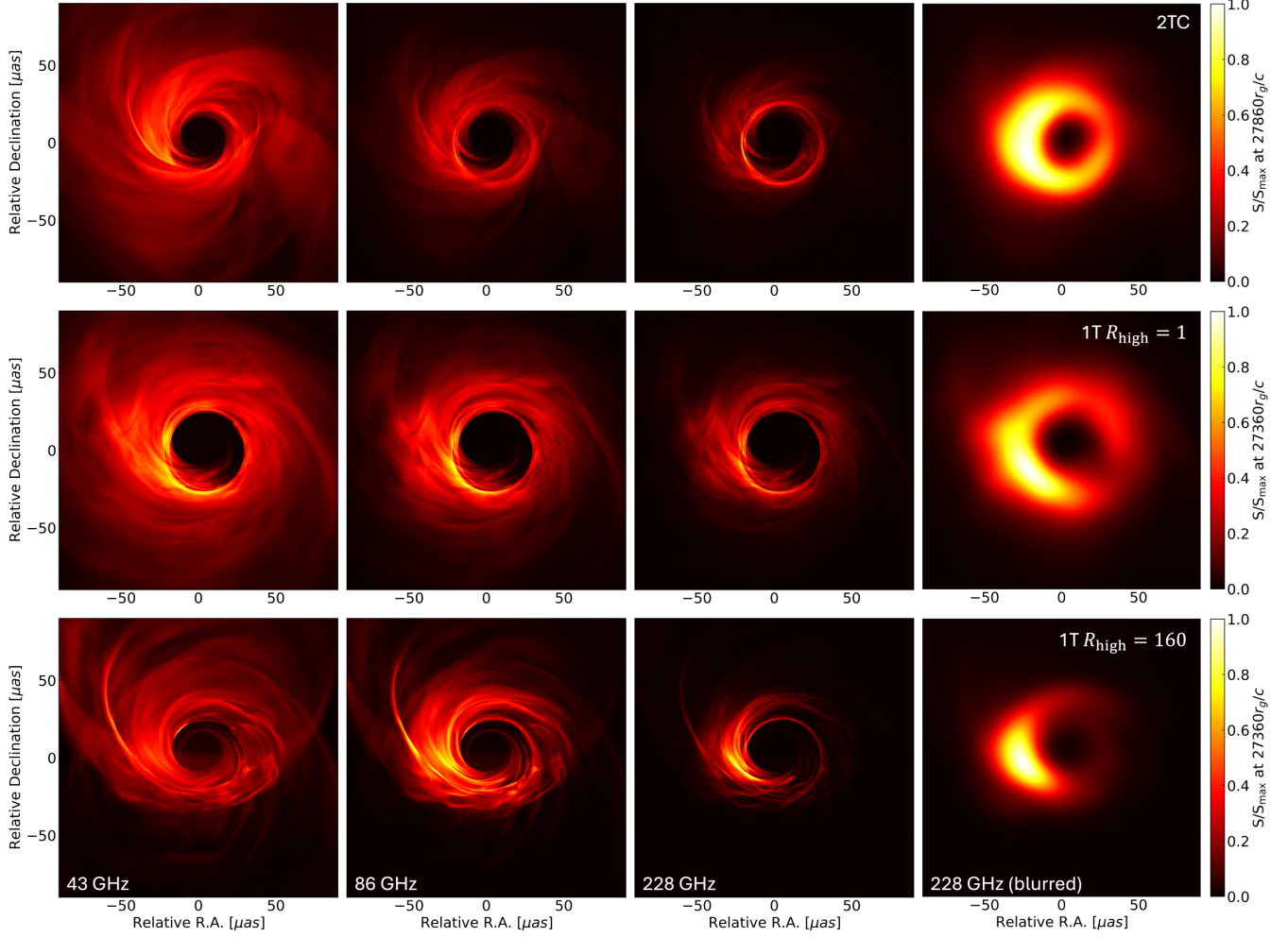
Figure 6. Ray-traced images at inclination 30°. Top row: 2TC simulation. Middle row: 1T simulation for $R_{\rm high} = 1$. Bottom row: 1T simulation for $R_{\rm high} = 160$. From left to right: 43, 86, 228 GHz (unblurred), and 228 GHz (blurred with a Gaussian kernel with FWHM = 15μas to simulate the resolution of the EHT). The mildly relativistic outflow in the disk-jet boundary is more visible for $R_{\rm high} = 160$. The accretion flow transitions from optically thick at 43-86 GHz to optically thin at 228-345-1360 GHz. Therefore, the synchrotron radiation variability increases with frequency as shown in Table 3. Images from the 2T simulation are not included here, as they are nearly identical to those from the 2TC simulation.

predictions per simulation: one using the evolved T_e directly from the simulation, and another where the evolved T_e is ignored and instead calculated in post-processing with the $R(\beta)$ prescription. We find that M_3 is lower when using the evolved T_e, suggesting that the T_e derived from the $R(\beta)$ prescription exhibits greater fluctuations (see Fig 7).

3.4 Fluctuations in electron and ion temperatures

In the $R(\beta)$ prescriptions used in 1T simulations, T_e fluctuates as much as T_i in regions with $\beta \gtrsim 1$ or $\lesssim 10^{-2}$ where $T_e \approx T_i/R$ (Moś-cibrodzka et al. 2016). However, that is not the case in a 2T treatment with different adiabatic indices for electrons and ions. Thermodynamically, a 2T treatment with $\gamma_e \neq \gamma_i$ is expected to have an impact in the fluctuation of T_e (private communication, Gammie, 2024). From the first law of thermodynamics, the convective derivatives of T_e and T_i are:

$$\frac{D \ln T_e}{Dt} = \frac{\gamma_e - 1}{k n_e T_e} q_e + \frac{\gamma_e - 1}{\tau_{\rm comp}} , \tag{22}$$

$$\frac{D \ln T_i}{Dt} = \frac{\gamma_i - 1}{k n_i T_i} q_i + \frac{\gamma_i - 1}{\tau_{\rm comp}} , \tag{23}$$

where the heating/cooling rate per unit volume $q = q^{\rm v} + q^C + q^-$ includes ion-electron energy exchange q^C, dissipation heating rate $q^{\rm v}$ and cooling rate q^-. For each species $q_e^{\rm v} = \delta_e q^{\rm v}$ and $q_i^{\rm v} = \delta_i q^{\rm v}$, with $\delta_e + \delta_i = 1$ and the total dissipation rate $q^{\rm v} = (u_e + u_i)/\tau_{\rm diss}$. We consider only radiative cooling of electrons, i.e. $q_e^- = u_e/\tau_{\rm cool}$ and $q_i^- = 0$. $\tau_{\rm comp}, \tau_{\rm diss}, \tau_{\rm cool}$ are the timescales of compression, dissipation, and cooling, respectively.

From our simulations $\gamma_e \approx 4/3$, $\gamma_i \approx 5/3$, $T_i/T_e \approx 3$, $\delta_e \approx [0.2 - 0.4]$, and $\delta_i \approx [0.8 - 0.6]$. Analysing the adiabatic process case $q = 0$, from Eq. (22) and (23), T_e fluctuates approximately half as much as T_i,

$$\frac{D \ln T_e}{Dt} = \frac{\gamma_e - 1}{\gamma_i - 1} \frac{D \ln T_i}{Dt} \approx \frac{1}{2} \frac{D \ln T_i}{Dt} , \tag{24}$$
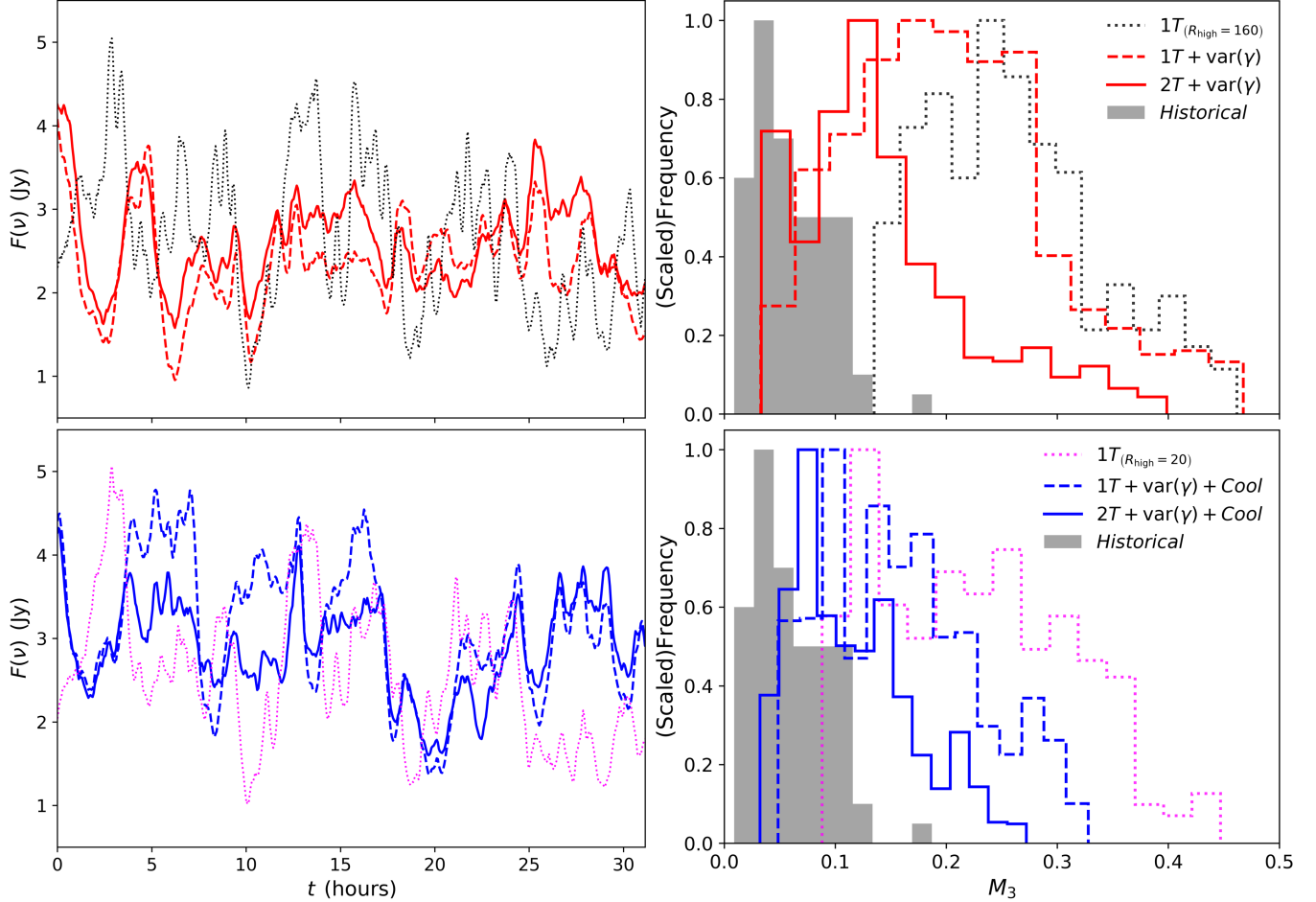
Figure 7. Light curves at 228 GHz (left panels) and M_3 distributions (right panels) at an inclination of $30°$. The 1T simulations are shown with dotted lines for $R_{high} = 20$ (magenta) and 160 (black). The 2T simulations are represented without cooling (red) and with cooling (blue). Solid lines indicate when the evolved T_e is directly taken from the 2T GRMHD simulations, while dashed lines indicate when the evolved T_e is ignored and instead calculated in post-process using the $R(\beta)$ prescription. Historical M_3 observations are shown in grey (Wielgus et al. 2022 and references therein). The 2T treatment with variable adiabatic index and the inclusion of radiative cooling brings the models closer to historical variability levels. Additionally, M_3 is lower when using the evolved T_e, indicating that the T_e derived from the $R(\beta)$ prescription exhibits greater fluctuations.

in the incompressible case $\tau_{comp} \to \infty$ with only heating,

$$\frac{D \ln T_e}{Dt} = \frac{\gamma_e - 1}{\gamma_i - 1} \frac{T_i}{T_e} \frac{\delta_e}{\delta_i} \frac{D \ln T_i}{Dt} \approx [0.4 - 1] \frac{D \ln T_i}{Dt} , \quad (25)$$

and the addition of cooling can reduce the fluctuations of T_e as compared to T_i,

$$\frac{D \ln T_e}{Dt} = \frac{\gamma_e - 1}{\gamma_i - 1} \frac{T_i}{T_e} \left(\frac{\delta_e}{\delta_i} - \frac{\tau_{diss}}{\tau_{cool}} \frac{u_e}{\delta_i(u_i + u_e)} \right) \frac{D \ln T_i}{Dt} . \quad (26)$$

Therefore, the difference in adiabatic indices between relativistic electrons and non-relativistic ions causes an effective reduction in the fluctuations of the electron temperature. This theoretically framework is in agreement with our results of M_3 distributions presented in Fig 7 and Table 3, and it aligns with our interpretation that the evolved T_e in 2T simulations with variable adiabatic indices fluctuates less than the T_e derived from the $R(\beta)$ prescription.

3.5 Comparison to semi-analytical models

In MAD states, we find substantial heating and synchrotron radiative cooling in areas with significant gas compression and high magnetisation. Our results for radiative efficiency align with those of

Liska et al. (2024), and challenge the paradigm in ADAF models, with low η_{rad} across all radii. In our 2T and 2TC simulations, we obtain $\langle T_e \rangle \approx 10^{11}$K, time averaged between $[16 - 29] \times 10^3 r_g/c$ and measured at $10r_g$, consistent with the values reported in spectral fitting modelling (e.g. Dexter et al. 2010; Markoff et al. 2001; Yuan et al. 2002) and EHT polarisation modelling (Dexter 2016; EHTC Sgr A*2017 V; EHTC Sgr A*2017 VIII).

In the ADAF model by Narayan et al. (1995), the radiative efficiency η_{rad} is less than 0.001 at all radii, meaning that less than 0.1% of the available accretion energy is radiated, with the flow being advection-dominated. For $r < 200r_g$, ion-electron coupling weakens, causing T_e to saturate, while T_i continues to follow the virial temperature profile. They found that T_e rises up to $\sim 10^{10}$K in accreting black hole flows. For Sgr A*, Quataert & Narayan (1999) achieved a good spectral fit using radiatively inefficient accretion flow (RIAF) models with $\delta_e = 0.55$ and required $T_e \sim 10^{11}$K close to the BH, which is larger than in ADAF models. In semi-analytical jet models of Sgr A*, Markoff et al. (2001) and Yuan et al. (2002) obtained a good spectral fit with electron temperatures reaching $\sim 10^{11}$K.

Recently, the EHTC reported a large resolved polarisation fraction of 24–28%, with a peak around 40% (EHTC Sgr A*2017 VII).

Table 3. Comparison of M_3 values at different frequencies for an inclination of 30°. As frequency increases, M_3 also increases due to the accretion flow becoming more optically thin. The inclusion of 2T treatment, variable adiabatic index, and radiative cooling of electrons reduces M_3.

ν (GHz)	Level of physics	M_3
43	1T	0.08 ± 0.04
43	1T+var(γ)	0.11 ± 0.04
43	1T+var(γ)+Cool	0.09 ± 0.04
43	2T+var(γ)	0.06 ± 0.03
43	2T+var(γ)+Cool	0.05 ± 0.02
86	1T	0.12 ± 0.05
86	1T+var(γ)	0.15 ± 0.07
86	1T+var(γ)+Cool	0.12 ± 0.05
86	2T+var(γ)	0.09 ± 0.05
86	2T+var(γ)+Cool	0.07 ± 0.04
228	1T	0.23 ± 0.09
228	1T+var(γ)	0.21 ± 0.09
228	1T+var(γ)+Cool	0.16 ± 0.07
228	2T+var(γ)	0.14 ± 0.08
228	2T+var(γ)+Cool	0.12 ± 0.05
345	1T	0.26 ± 0.10
345	1T+var(γ)	0.22 ± 0.10
345	1T+var(γ)+Cool	0.17 ± 0.07
345	2T+var(γ)	0.16 ± 0.09
345	2T+var(γ)+Cool	0.13 ± 0.06
1360	1T	0.32 ± 0.11
1360	1T+var(γ)	0.27 ± 0.11
1360	1T+var(γ)+Cool	0.21 ± 0.08
1360	2T+var(γ)	0.21 ± 0.11
1360	2T+var(γ)+Cool	0.16 ± 0.07

Synchrotron emission is intrinsically highly polarised, but as light traverses a magnetised medium, it undergoes Faraday depolarisation (e.g. Ricarte et al. 2020). Faraday depth, which quantifies the rotation of polarised light, is inversely proportional to T_e^2 (Jones & Hardee 1979). Consequently, higher T_e leads to reduced depolarisation. In one-zone models, the total flux and optical depth constraints for Sgr A* indicate small Faraday depths, which account for the high polarisation fraction. Based on estimates of $n_e \approx 10^6 \, \mathrm{cm}^{-3}$ and $B \approx 29 \, \mathrm{G}$, it is expected that $T_e \approx 10^{11} \, \mathrm{K}$ at $\beta = 1$ (Dexter 2016; EHTC Sgr A*2017 V; EHTC Sgr A*2017 VIII), consistent with our results. Locally, β_i can drop below unity, particularly at the disk-jet interface and within flux tubes. However, the time-averaged $\langle \beta_i \rangle \approx 1$ in the disk at $\lesssim 20 r_g$, as shown in Fig. 4.

4 CONCLUSIONS

The EHTC has provided significant insights into the Galactic center source Sgr A*. Models based on 1T GRMHD simulations have been able to explain aspects of observations across radio to X-ray wavelengths in quiescent (EHTC Sgr A*2017 V; EHTC Sgr A*2017 VIII), and flaring states (e.g. Chatterjee et al. 2021; Scepi et al. 2022). However, none of the EHTC ray-traced models fully satisfy all the constraints drawn from multiwavelength observations at 86 GHz, 230 GHz, 2.2 μm, and in the X-ray (EHTC Sgr A*2017 II; EHTC Sgr A*2017 VII). The 230 GHz variability constraint is particularly stringent, as nearly all EHTC models in a MAD state exhibit greater variability (EHTC Sgr A*2017 V) than historical observations (Wielgus

et al. 2022 and references therein). This limitation is possibly attributed to the modelled prescription of T_i/T_e, which is based on the local plasma magnetisation (so called $R(\beta)$ prescriptions, e.g. Mościbrodzka et al. 2016; Anantua et al. 2020). In reality, T_e is fundamentally influenced by microphysical plasma and radiation interactions, and does not depend trivially on T_i. A first-principles kinetic approach is required to model these collisionless effects (Parfrey et al. 2019; Crinquand et al. 2022; Galishnikova et al. 2023a).

Our investigation into 2T thermodynamics within MAD GRMHD simulations addresses some of these limitations by evolving both electron and ion temperatures (Ressler et al. 2015; Sądowski et al. 2017). We do not resolve the actual heating mechanisms; instead, we assume that heating at the grid scale occurs through sub-grid magnetic reconnection (Rowan et al. 2017). We do not model non-thermal electron distributions which are likely non-negligible (Moscibrodzka 2024). We perform an analysis of variability that systematically adds one layer of physics at a time (see Table 3). By incorporating the 2T treatment, variable adiabatic index, and radiative cooling of electrons, we achieve a closer match to historical 228 GHz variability compared to 1T simulations. We find an effective reduction of nearly 50% in the values of the three-hour modulation index (M_3) distribution. Additionally, we find that M_3 increases with frequency and does not significantly depend on the angle between the observer's line of sight and the angular momentum vector of the accretion disk.

In a 2T GRMHD simulation, we extract two light curve predictions: one using the evolved T_e directly from the simulation, and another where the evolved T_e is ignored and instead calculated in post-processing with the $R(\beta)$ prescription. We find that M_3 is lower when using the evolved T_e, suggesting that the T_e derived from the $R(\beta)$ prescription exhibits greater fluctuations (see Fig. 7). This result is consistent with theoretical expectations for a 2T treatment, where the difference in adiabatic indices between relativistic electrons and non-relativistic ions causes an effective reduction in the fluctuations of the electron temperature (see section 3.4).

Even for the very low accretion rates relevant for Sgr A* ($f_{\mathrm{edd}} \approx 10^{-7}$), we find that radiative cooling of electrons—via synchrotron, inverse Compton, and bremsstrahlung processes—still affects the accretion flow, lowering T_e in the inner $50 r_g$ accretion disk (see Fig. 5), reducing average 228 GHz synchrotron flux, and shifting the M_3 distribution towards lower variability values by roughly 10%. We find that synchrotron emission dominates over inverse Compton, while bremsstrahlung is negligible, consistent with Yoon et al. (2020). Our estimated radiative efficiency, $\eta_{\mathrm{rad}} \approx [0.02 - 0.05]$, is broadly consistent with the value $\eta_{\mathrm{rad}} \approx 0.03$ obtained from GRRMHD MAD simulations that include radiative transport (Liska et al. 2024). These results challenge the paradigm in ADAF models, with $\eta_{\mathrm{rad}} < 0.001$ across all radii. MAD states have higher radiative efficiency, while in SANE states, cooling is expected to be less significant especially at low accretion rates. Therefore, electron radiative cooling is non negligible if the accretion flow of Sgr A* has a dynamically strong magnetic field, typical of a MAD state, as favoured by the current EHT observations.

Despite these improvements, further progress is required, as our 2T simulations still show more variability than historical observations of Sgr A*. For example, the more realistic stellar wind-fed accretion models better predict the submillimetre variability due to the comparatively lower levels of small-scale turbulence compared to SANE and MAD models (Murchikova et al. 2022). Additionally, our simulations do not resolve plasmoid-mediated magnetic reconnection, that requires higher resolution (Salas et al. 2024) or an effective resistivity or viscosity. Magnetic reconnection can cause the dissipation of magnetic energy into heat (Ripperda et al. 2019, 2022),

thereby potentially influencing the radiative efficiency. Furthermore, ideal magnetohydrodynamics can never capture kinetic effects, like pressure anisotropy that can influence synchrotron emission and absorption (Galishnikova et al. 2023a,b). An inherent uncertainty in our approach stems from not resolving the heating mechanisms and relying on a single heating prescription. In future work we will explore heating prescriptions based on first-principles kinetic simulations in particular regions of the GRMHD domain, approximating a number of important subgrid effects of collisionless physics not captured by GRMHD simulations.

ACKNOWLEDGEMENTS

DATA AVAILABILITY

The simulation post-processed data used to plot the images in this work are available in Zenodo at http://doi.org/10.5281/zenodo.14793884.

REFERENCES

Agol E., 2000, ApJ, 538, L121
Anantua R., Ressler S., Quaataert E., 2020, MNRAS, 493, 1404
Balick B., Brown R. L., 1974, ApJ, 194, 265
Bisnovatyi-Kogan G. S., Ruzmaikin A. A., 1974, Ap&SS, 28, 45
Bower G. C., Wright M. C. H., Falcke H., Backer D. C., 2003, ApJ, 588, 331
Bower G. C., et al., 2018, ApJ, 868, 101
Bower G. C., et al., 2019, ApJ, 881, L2
Chael A., 2025, arXiv e-prints, p. arXiv:2501.12448
Chael A., Rowan M., Narayan R., Johnson M., Sironi L., 2018, MNRAS, 478, 5209
Chael A., Narayan R., Johnson M. D., 2019, MNRAS, 486, 2873
Chatterjee K., Narayan R., 2022, ApJ, 941, 30
Chatterjee K., et al., 2021, MNRAS, 507, 5281
Crinquand B., Cerutti B., Dubus G., Parfrey K., Philippov A., 2022, Phys. Rev. Lett., 129, 205101
Davelaar J., Moscibrodzka M., Bronzwaer T., Falcke H., 2018, Astronomy and Astrophysics, 612
Dexter J., 2016, MNRAS, 462, 115
Dexter J., Agol E., Fragile P. C., McKinney J. C., 2010, ApJ, 717, 1092
Dexter J., Kelly B., Bower G. C., Marrone D. P., Stone J., Plambeck R., 2014, MNRAS, 442, 2797
Dexter J., et al., 2020, MNRAS, 494, 4168
Dexter J., Scepi N., Begelman M. C., 2021, ApJ, 919, L20
Dibi S., Drappeau S., Fragile P. C., Markoff S., Dexter J., 2012, MNRAS, 426, 1928
Dihingia I. K., Mizuno Y., Fromm C. M., Rezzolla L., 2023, MNRAS, 518, 405
Do T., et al., 2019, Science, 365, 664
Drappeau S., Dibi S., Dexter J., Markoff S., Fragile P. C., 2013, MNRAS, 431, 2872
Ekers R. D., Goss W. M., Schwarz U. J., Downes D., Rogstad D. H., 1975, A&A, 43, 159
Esin A. A., Narayan R., Ostriker E., Yi I., 1996, ApJ, 465, 312
Esin A. A., McClintock J. E., Narayan R., 1997, ApJ, 489, 865
Event Horizon Telescope Collaboration et al., 2022a, ApJ, 930, L12
Event Horizon Telescope Collaboration et al., 2022b, ApJ, 930, L13
Event Horizon Telescope Collaboration et al., 2022c, ApJ, 930, L16
Event Horizon Telescope Collaboration et al., 2024a, ApJ, 964, L25
Event Horizon Telescope Collaboration et al., 2024b, ApJ, 964, L26
Fazio G. G., et al., 2018, ApJ, 864, 58
Fishbone L. G., Moncrief V., 1976, The Astrophysical Journal, 207, 962
Fragile P. C., Meier D. L., 2009, ApJ, 693, 771
GRAVITY Collaboration et al., 2018, A&A, 615, L15
GRAVITY Collaboration et al., 2019, A&A, 625, L10
Galishnikova A., Philippov A., Quataert E., Bacchini F., Parfrey K., Ripperda B., 2023a, Phys. Rev. Lett., 130, 115201
Galishnikova A., Philippov A., Quataert E., 2023b, ApJ, 957, 103
Galishnikova A., Philippov A., Quataert E., Chatterjee K., Liska M., 2025, ApJ, 978, 148
Gammie C. F., McKinney J. C., Tóth G., 2003, ApJ, 589, 444
Ghez A. M., et al., 2003, ApJ, 586, L127
Ghez A. M., et al., 2008, ApJ, 689, 1044
Gillessen S., Eisenhauer F., Trippe S., Alexander T., Genzel R., Martins F., Ott T., 2009, ApJ, 692, 1075
Howes G. G., 2010, MNRAS, 409, L104
Iwata Y., Oka T., Tsuboi M., Miyoshi M., Takekawa S., 2020, ApJ, 892, L30
Jones T. W., Hardee P. E., 1979, ApJ, 228, 268
Kawazura Y., Barnes M., Schekochihin A. A., 2019, Proceedings of the National Academy of Science, 116, 771
Lalakos A., Tchekhovskoy A., Bromberg O., Gottlieb O., Jacquemin-Ide J., Liska M., Zhang H., 2024, ApJ, 964, 79
Liska M. T. P., et al., 2022, ApJS, 263, 26
Liska M. T. P., Kaaz N., Chatterjee K., Emami R., Musoke G., 2024, ApJ, 966, 47
Lo K. Y., Schilizzi R. T., Cohen M. H., Ross H. N., 1975, ApJ, 202, L63
Mahadevan R., Quataert E., 1997, ApJ, 490, 605
Markoff S., Falcke H., Yuan F., Biermann P. L., 2001, A&A, 379, L13
Marrone D. P., Moran J. M., Zhao J.-H., Rao R., 2006, in Journal of Physics Conference Series. pp 354–362 (arXiv:astro-ph/0607432), doi:10.1088/1742-6596/54/1/056
Marrone D. P., Moran J. M., Zhao J.-H., Rao R., 2007, ApJ, 654, L57
Marrone D. P., et al., 2008, ApJ, 682, 373
McKinney J. C., Tchekhovskoy A., Blandford R. D., 2012, MNRAS, 423, 3083
Mizuno Y., Fromm C. M., Younsi Z., Porth O., Olivares H., Rezzolla L., 2021, MNRAS, 506, 741
Moscibrodzka M., 2024, arXiv e-prints, p. arXiv:2412.06492
Mościbrodzka M., Gammie C. F., Dolence J. C., Shiokawa H., Leung P. K., 2009, ApJ, 706, 497
Mościbrodzka M., Falcke H., Shiokawa H., 2016, A&A, 586, A38

Mościbrodzka M., Dexter J., Davelaar J., Falcke H., 2017, MNRAS, 468, 2214

Murchikova L., Witzel G., 2021, ApJ, 920, L7

Murchikova L., White C. J., Ressler S. M., 2022, ApJ, 932, L21

Narayan R., Yi I., 1994, ApJ, 428, L13

Narayan R., Yi I., Mahadevan R., 1995, Nature, 374, 623

Narayan R., Igumenshchev I. V., Abramowicz M. A., 2003, PASJ, 55, L69

Narayan R., Kumar P., Tchekhovskoy A., 2011, MNRAS, 416, 2193

Narayan R., SÄ dowski A., Penna R. F., Kulkarni A. K., 2012, MNRAS, 426, 3241

Noble S. C., Gammie C. F., McKinney J. C., Del Zanna L., 2006, ApJ, 641, 626

Novikov I. D., Thorne K. S., 1973, in Black Holes (Les Astres Occlus). pp 343–450

Parfrey K., Philippov A., Cerutti B., 2019, Phys. Rev. Lett., 122, 035101

Porth O., Mizuno Y., Younsi Z., Fromm C. M., 2021, MNRAS, 502, 2023

Quataert E., 1998, ApJ, 500, 978

Quataert E., Narayan R., 1999, ApJ, 520, 298

Rees M. J., Begelman M. C., Blandford R. D., Phinney E. S., 1982, Nature, 295, 17

Ressler S. M., Tchekhovskoy A., Quataert E., Chandra M., Gammie C. F., 2015, MNRAS, 454, 1848

Ressler S. M., Tchekhovskoy A., Quataert E., Gammie C. F., 2017, MNRAS, 467, 3604

Ressler S. M., White C. J., Quataert E., Stone J. M., 2020, ApJ, 896, L6

Ressler S. M., Quataert E., White C. J., Blaes O., 2021, MNRAS, 504, 6076

Ressler S. M., White C. J., Quataert E., 2023, MNRAS, 521, 4277

Ricarte A., Prather B. S., Wong G. N., Narayan R., Gammie C., Johnson M. D., 2020, MNRAS, 498, 5468

Ripperda B., et al., 2019, ApJS, 244, 10

Ripperda B., Liska M., Chatterjee K., Musoke G., Philippov A. A., Markoff S. B., Tchekhovskoy A., Younsi Z., 2022, ApJ, 924, L32

Rowan M. E., Sironi L., Narayan R., 2017, ApJ, 850, 29

Rowan M. E., Sironi L., Narayan R., 2019, ApJ, 873, 2

Ryan B. R., Dolence J. C., Gammie C. F., 2015, ApJ, 807, 31

Ryan B. R., Ressler S. M., Dolence J. C., Tchekhovskoy A., Gammie C., Quataert E., 2017, ApJ, 844, L24

Salas L. D. S., Musoke G., Chatterjee K., Markoff S. B., Porth O., Liska M. T. P., Ripperda B., 2024, MNRAS, 533, 254

Scepi N., Dexter J., Begelman M. C., 2022, MNRAS, 511, 3536

Schödel R., et al., 2002, Nature, 419, 694

Shapiro S. L., Lightman A. P., Eardley D. M., 1976, ApJ, 204, 187

Sądowski A., Wielgus M., Narayan R., Abarca D., McKinney J. C., Chael A., 2017, MNRAS, 466, 705

Stepney S., Guilbert P. W., 1983, MNRAS, 204, 1269

Tchekhovskoy A., Narayan R., McKinney J. C., 2011, MNRAS, 418, L79

Tchekhovskoy A., McKinney J. C., Narayan R., 2012, in Journal of Physics Conference Series. IOP, p. 012040 (arXiv:1202.2864), doi:10.1088/1742-6596/372/1/012040

Wielgus M., et al., 2022, ApJ, 930, L19

Witzel G., et al., 2021, ApJ, 917, 73

Yoon D., Chatterjee K., Markoff S. B., van Eijnnatten D., Younsi Z., Liska M., Tchekhovskoy A., 2020, MNRAS, 499, 3178

Younsi Z., Wu K., Fuerst S. V., 2012, A&A, 545, A13

Younsi Z., Zhidenko A., Rezzolla L., Konoplya R., Mizuno Y., 2016, Phys. Rev. D, 94, 084025

Yuan F., Markoff S., Falcke H., 2002, A&A, 383, 854

Yuan F., Quataert E., Narayan R., 2003, ApJ, 598, 301

Yusef-Zadeh F., et al., 2009, ApJ, 706, 348

APPENDIX A: COULOMB COUPLING

The transfer of energy between ions and electrons is characterised by the Coulomb coupling rate in the comoving frame, which in units of erg cm^{-3} s^{-1} is equivalent to,

$$q^C = \frac{3m_e}{2m_i} \bar{n} n_e \ln\Lambda \frac{ck\sigma_T (T_i - T_e)}{K_2(1/\theta_i) K_2(1/\theta_e)}$$
$$\times \left[\frac{2(\theta_e + \theta_i)^2 + 1}{\theta_e + \theta_i} K_1(1/\theta_m) + 2K_0(1/\theta_m) \right],$$

(A1)

with $\theta_m = (1/\theta_e + 1/\theta_i)^{-1}$ and $m_i = m_p (X + 4Y)$. K_i is the modified Bessel function of the ith order, $\ln\Lambda \approx 20$ is the Coulomb logarithm, and $\bar{n} = (X + Y)\rho/m_p$ is the number density (Stepney & Guilbert 1983; Sądowski et al. 2017). Ryan et al. (2017) suggested that Coulomb collisions become as important as viscous heating at $f_{\rm edd} \approx 10^{-4}$. Dexter et al. (2021) and Liska et al. (2024) found Coulomb collisions are not important until $f_{\rm edd} \approx 10^{-3}$. Conversely, semi-analytical models typically assume that Coulomb collisions dominate for $f_{\rm edd} \gtrsim 10^{-2}$ (Esin et al. 1997).

This paper has been typeset from a TeX/LaTeX file prepared by the author.